Available online at www.sciencedirect.com
ScienceDirect
Icarus 189 (2007) 479–492
ICARUS
www.elsevier.com/locate/icarus

Saturn eddy momentum fluxes and convection: First estimates from Cassini images

Anthony D. Del Genio [a,*], John M. Barbara [b], Joseph Ferrier [b], Andrew P. Ingersoll [c], Robert A. West [d], Ashwin R. Vasavada [d], Joseph Spitale [e], Carolyn C. Porco [e]

[a] *NASA Goddard Institute for Space Studies, 2880 Broadway, New York, NY 10025, USA*
[b] *Sigma Space Partners, LLC, Institute for Space Studies, 2880 Broadway, New York, NY 10025, USA*
[c] *Division of Geological and Planetary Sciences, California Institute of Technology, 150-21, Pasadena, CA 91125, USA*
[d] *Jet Propulsion Laboratory, California Institute of Technology, 4800 Oak Grove Drive, Pasadena, CA 91109, USA*
[e] *Cassini Imaging Central Laboratory for Operations, Space Science Institute, 4750 Walnut Street, Suite 205, Boulder, CO 80301, USA*

Received 26 June 2006; revised 28 November 2006

Available online 16 March 2007

Abstract

We apply an automated cloud feature tracking algorithm to estimate eddy momentum fluxes in Saturn's southern hemisphere from Cassini Imaging Science Subsystem near-infrared continuum image sequences. Voyager Saturn manually tracked images had suggested no conversion of eddy to mean flow kinetic energy, but this was based on a small sample of <1000 wind vectors. The automated procedure we use for the Cassini data produces an order of magnitude more usable wind vectors with relatively unbiased sampling. Automated tracking is successful in and around the westward jet latitudes on Saturn but not in the vicinity of most eastward jets, where the linearity and non-discrete nature of cloud features produces ambiguous results. For the regions we are able to track, we find peak eddy fluxes $\sim 10\ \mathrm{m^2\,s^{-2}}$ and a clear positive correlation between eddy momentum fluxes and meridional shear of the mean zonal wind, implying that eddies supply momentum to eastward jets and remove momentum from westward jets at a rate $\sim 5 \times 10^{-6}\ \mathrm{m\,s^{-2}}$. The behavior we observe is similar to that seen on Jupiter, though with smaller eddy-mean kinetic energy conversion rates per unit mass of atmosphere ($3.3 \times 10^{-5}\ \mathrm{m^2\,s^{-3}}$). We also use the appearance and rapid evolution of small bright features at continuum wavelengths, in combination with evidence from weak methane band images where possible, to diagnose the occurrence of moist convective storms on Saturn. Areal expansion rates imply updraft speeds of $\sim 1\ \mathrm{m\,s^{-1}}$ over the convective anvil cloud area. As on Jupiter, convection preferentially occurs in cyclonic shear regions on Saturn, but unlike Jupiter, convection is also observed in eastward jet regions. With one possible exception, the large eddy fluxes seen in the cyclonic shear latitudes do not seem to be associated with convective events.

Keywords: Saturn, atmosphere; Atmospheres, dynamics; Meteorology; Jovian planets

1. Introduction

The defining dynamical property of the atmospheres of Jupiter and Saturn is their system of multiple alternating eastward and westward jets. On Jupiter, the horizontal shear regions between the jets are well-correlated with zonally oriented cloud albedo features ("belts" and "zones") that have been interpreted in terms of the sense of large-scale vertical motion (Hess and Panofsky, 1951; Ingersoll and Cuzzi, 1969); on Saturn a less consistent relationship between winds and clouds exists (Smith et al., 1981). Aside from Saturn's equatorial jet region, which may be variable in strength and/or cloud vertical structure (Sánchez-Lavega et al., 2004), and the 23° N jet on Jupiter (García-Melendo and Sánchez-Lavega, 2001), the other jets on both planets have been remarkably stable over several decades (Porco et al., 2003, 2005).

One of the major challenges to our understanding of these planets is to define the physical processes responsible for the maintenance of the jets and the banded cloud structure. Pro-

* Corresponding author. Fax: +1 212 678 5552.
E-mail address: adelgenio@giss.nasa.gov (A.D. Del Genio).

0019-1035/$ – see front matter
doi:10.1016/j.icarus.2007.02.013

posed mechanisms invoke either deep convective cylinders or shallow weather layer phenomena such as barotropic or baroclinic instability or moist convection as the ultimate source of energy for the jets (see Vasavada and Showman, 2005 for a review). Few observational constraints beyond the magnitude and spacing of the jets currently exist, though. In general, forcing for the mean zonal flow can consist of accelerations due to thermally direct mean meridional circulations associated with diabatic heating, or due to indirect circulations that respond to eddy momentum or heat flux convergences.

In recent years the Galileo and Cassini missions have provided some initial insights into these issues for Jupiter. For example, the assumed sense of the mean meridional overturning circulation, with rising motion in the bright zones and sinking motion in the darker belts, has been called into question by the finding that deep moist convective cloud features and lightning, and thus upwelling at the water condensation level, are restricted to the cyclonically sheared belt regions (Ingersoll et al., 2000; Porco et al., 2003). This would require an indirect circulation and thus a source of eddy forcing of the circulation. Early Voyager analyses of manually tracked cloud features implying horizontal eddy momentum flux convergence into the jets (Beebe et al., 1980; Ingersoll et al., 1981), which would be consistent with rising motion in the belts, were cast into doubt by Sromovsky et al. (1982). However, a more evenly sampled dataset of twice the size gave a similar result (Mitchell, 1982), and a recent automated tracking study of a much larger Cassini Jupiter flyby dataset, including analyses of various possible error sources, appears to support the original conclusion, albeit with a 2–4 times smaller inferred magnitude of the eddy-zonal kinetic energy conversion (Salyk et al., 2006).

On Saturn, however, the situation is less clear because the inherently lower image feature contrast limits the number of useful candidates for tracking. Ingersoll et al. (1984) and Sromovsky et al. (1986) attempted to derive eddy momentum fluxes from low-resolution Voyager flyby images, both finding negligible correlations between the eddy flux and the meridional shear of the zonal flow. Sromovsky et al. (1983) show mean meridional flow estimates for Saturn's northern hemisphere, including one westward jet with apparent mean flow divergence at cloud top but little systematic behavior elsewhere. Thus, few if any constraints on Saturn's large-scale dynamics at cloud level, other than the sense of the jets themselves, currently exist.

The Imaging Science Subsystem (ISS) experiment on the Cassini Orbiter mission (Porco et al., 2004) presents an opportunity to revisit these questions for Saturn with higher resolution, higher quality data over an extended period of time that will allow for climatologically representative estimates of eddy-mean flow interactions to be acquired. Initial assessments of the mean Saturn flow and its vertical structure (Porco et al., 2005) and distributions of vortices and spots (Vasavada et al., 2006) have been presented. In this paper we apply an automated cloud tracking technique to make an initial estimate of eddy momentum fluxes on Saturn. We also survey the distribution of convective features and assess the possibility of their role in the processes that maintain the jets on Saturn. The paper is organized as follows. Section 2 describes the dataset, processing, tracking algorithm, and convective feature identification approach. Eddy momentum flux distributions, their relationship to the mean flow, and tests of the sensitivity of the results to the tracking assumptions are described in Section 3. Convective feature identification, evolution, and relationship to the mean flow are explored in Section 4. We summarize our results and discuss their implications for ideas about the maintenance of the Saturn general circulation in Section 5.

2. Data and methods

2.1. Image selection and processing

We analyze 20 pairs of cylindrically projected ISS images separated by one planetary rotation obtained early in the Cassini orbital tour (5–8 February 2005), covering nearly 4 Saturn rotations at 19 km pixel^{-1} raw resolution. An imaging gap occurred in the middle of the period so that two independent sets of image pairs are available for each location observed. The images were acquired near apoapsis as part of a series of 3 × 3 mosaics covering most of Saturn's southern hemisphere, with a subspacecraft latitude of 5° S and a subsolar latitude of 19° S. Obstruction and shading of the northern hemisphere by Saturn's rings at this spacecraft and illumination geometry limit our analysis to the southern hemisphere. Individual frames near the limb and terminator were excluded from the analysis to minimize errors due to foreshortening and variations in seeing level. The images we analyze were acquired in a near-infrared continuum (CB2, 750 nm effective wavelength) filter that provides maximum feature contrast.

Images were flux calibrated using Cassini Imaging Science Subsystem CALibration (CISSCAL) software described in Porco et al. (2004). CISSCAL reads raw images, subtracts dark current and bias, divides by a flat field, corrects for nonlinearity and for the presence of a dust ring in the narrow angle camera field of view, and converts to I/F units. For filter combinations where absolute calibration has been possible, it applies another correction factor to bring results into line with that absolute calibration. A Minnaert function was applied to correct for large-scale illumination gradients before the images were cylindrically projected into 0.02 degree pixel^{-1} arrays, or ∼21 km pixel^{-1} at the equator. High-resolution narrow-angle images are navigated using IDL-based Modular Image and NAvigation Software (MINAS) developed at the Cassini Imaging Central Laboratory for Operations. MINAS reads various image formats, plots limb, ring, center, planet and ring grids, and star positions, accounts for ring obscuration, and fits limb and ring edges and star positions to correct camera pointing and enable mapping of globe surfaces. For our navigation of narrow-angle images, MINAS exploits near simultaneous wide-angle images that provide a visible planetary limb. Wide-angle images are scanned to locate the limb with sub-pixel precision. Approximate predicted pointing, extracted from binary C-kernels, is then matched to the scanned curve with a linear least-squares fit. Finally, a small boresight correction is applied to account for the known offset between the ISS Wide Angle and Narrow Angle Cameras. Navigated images are then

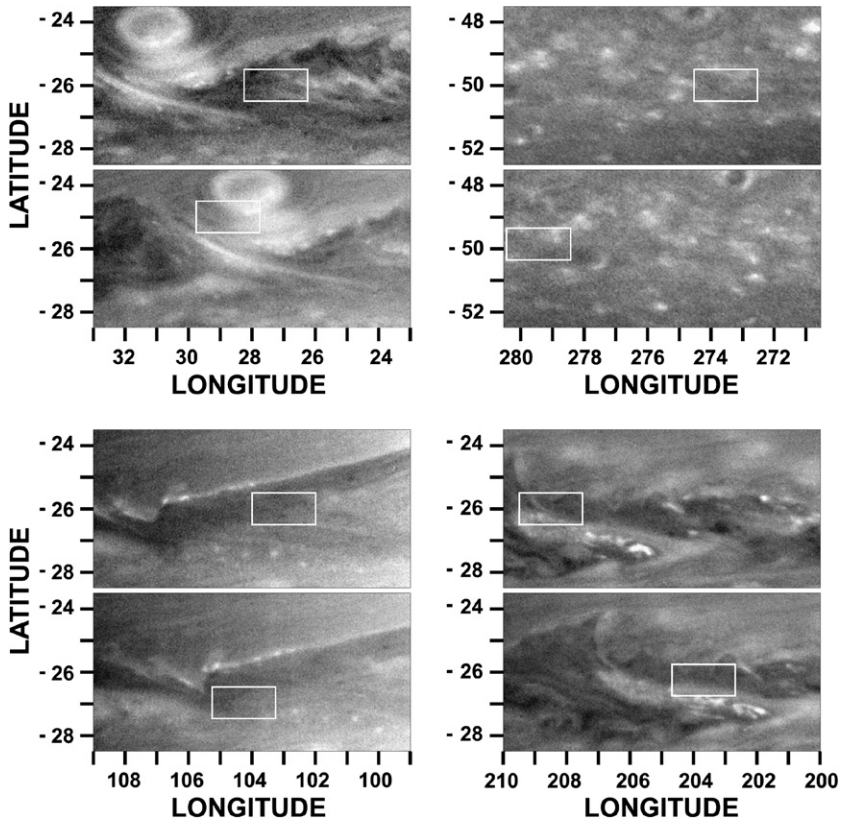

Fig. 1. Examples of four albedo patterns that produce spurious feature tracks. The upper and lower frames of each pair are separated by one rotation. The white rectangle indicates the tracking box in the first image and the location of peak correlation in the second image.

mapped into a simple cylindrical (rectangular) projection in the planetocentric latitude system.

2.2. Automated cloud tracking algorithm

Winds are measured using an automated tracking technique adapted from that originally developed for Pioneer Venus (Rossow et al., 1990). Evenly spaced 100 × 50 pixel (2° × 1°) target boxes are defined in the first of an image pair and a larger area of the second image is searched to find the location of maximum correlation between the two target arrays. The larger search region in the second image is an array of 700 × 150 pixels centered on the initial location in the first image. This allows for wind speeds up to ∼200 (∼40 $m\,s^{-1}$) of either sign in the zonal (meridional) direction. Step sizes between successive target boxes are 25 pixels (0.5°) in both latitude and longitude. We tested target boxes of various sizes (squares from 30 × 30 to 150 × 150 pixels, and rectangles from 40 × 10 to 200 × 100 pixels) but found that smaller target boxes, which work better for Jupiter, produce too many false matches for Saturn, while larger boxes visibly smooth the latitudinal profile of wind. The advantage of the automated technique is its objective selection of features and efficient survey of large numbers of images, which yields many more vectors than is possible with manual tracking. Its weakness is its susceptibility to spurious pattern matching in locations with repetitive or linear albedo patterns. As we describe below, this limits the application of the automated technique to certain latitude bands on Saturn.

For the nominal case, of the 21,021 vectors collected at latitudes where tracking was successful (see Section 3), ∼25% were rejected based on low correlation coefficients ($r < 0.5$). An additional 25% were rejected as spurious because either meridional or zonal displacements exceeded 1 standard deviation of the mean meridional or zonal wind speeds for the given latitude (see Fig. 1 and discussion below). This leaves 11,398 vectors in our nominal population. To put this into context, Ingersoll et al.'s (1984) null result for Saturn eddy momentum fluxes was based on only 882 manually tracked Voyager wind vectors. Our population size is comparable to that used for Voyager Jupiter eddy momentum flux estimates based on manual tracking (Beebe et al., 1980; Ingersoll et al., 1981) but an order of magnitude less than that acquired by Salyk et al. (2006) for their Cassini Jupiter estimate using an automated tracking procedure.

Fig. 1 illustrates the types of image features that fool the automated tracking program and produce spurious wind vectors. The upper left panels show two obviously unrelated features in the first and second images of the pair that share a general tendency for linear features oriented northwest to southeast within the target area. The upper right panels show a higher latitude region of chaotic features in which the algorithm focuses on the general increase in brightness from the southwest to the northeast corner of the target. The lower left and right panels show two examples of larger-scale adjacent bands of contrasting albedo in which the tracking program cannot differentiate among the various different positions along the albedo bound-

ary. These types of vectors produce a random distribution of wind speeds and tend to be especially noticeable in the meridional velocity field, since meridional winds are generally quite small on Saturn. Our one standard deviation rejection criteria eliminate most of these vectors, though occasional spurious vectors with implied wind speeds close to the real wind speeds exist and are retained (see Section 3).

The primary sources of uncertainty in wind estimates are due to pixel resolution, navigation error, and shape changes. For images separated by one Saturn rotation, pixel resolution limits our ability to discern velocity differences to $\sim$0.6 m s^{-1}. Navigation is performed to wide-angle image sub-pixel accuracy, formally $\sim$3 m s^{-1} if we take this to be half a wide-angle pixel or 5 narrow-angle pixels. In practice the navigation is usually better than this—matching seams of adjacent narrow-angle images suggests errors ranging from 0 to 4 pixels, i.e., the typical instantaneous error is $\sim$1 m s^{-1}. An indirect estimate of the accuracy of the navigation is provided by the mean meridional wind field, which should be zero integrated over the entire planet but can be biased by rotation errors that alias a fraction of the much larger zonal wind displacements into the meridional direction. For our dataset we derive a mean meridional wind of 0.2 m s^{-1} averaged over all latitudes, although as described below, our latitudinal sampling is incomplete. Thus, systematic bias due to rotation errors appears to be minimal. Shape changes are likely to be the largest source of instantaneous error and the hardest to quantify. Significant shape changes generally degrade the correlation between a pair of images, and so some indication of shape error may be obtained by eliminating our lowest correlation features. We find, for example, that restricting our dataset to only those features with correlation coefficient $r > 0.8$ produces a mean zonal wind field that differs from the nominal ($r > 0.5$) case by $\sim$2 m s^{-1} on average but as much as 10 m s^{-1} at latitudes where the tracking algorithm begins to fail (see Section 3). Stretching of linear features that tilt into the wind shear can potentially artificially enhance the correlation and the eddy momentum flux. Salyk et al. (2006) conclude that this may have a quantitative but not qualitative effect at a few latitudes on Jupiter; visual inspection of a subset of our Saturn wind vectors suggests that this is not as important as other sources of error.

2.3. Convective cloud feature identification

Convective clouds cannot uniquely be identified without direct sensing of an unstable lapse rate and strong upward vertical velocity. On Jupiter, circumstantial evidence for moist convection exists in the form of small-scale features with higher than average albedos at both continuum and methane band wavelengths, indicating clouds with high tops that are optically thick (Gierasch et al., 2000; Porco et al., 2003). Such features often appear and disappear on time scales of days and are usually adjacent to regions of low methane band brightness, consistent with the idea of rapid development in the updraft region and compensating subsidence that clears out at least the higher level clouds, and sometimes all clouds, and permits seeing to depth in surrounding areas. Occasional observations of lightning (Little et al., 1999; Dyudina et al., 2004) and humid regions at depth adjacent to such cloud features (Roos-Serote et al., 2002) reinforce the convective cloud interpretation.

On Saturn convective feature identification is more difficult than on Jupiter due to Saturn's colder atmosphere and thus deeper apparent condensation levels (Carlson et al., 1988), overlying tropospheric hazes (Karkoschka and Tomasko, 2005), and greater methane abundance above the clouds (West et al., 1982), which combine to make methane band filters less effective at height discrimination than on Jupiter. Furthermore, neither optical detection of lightning nor humidity observations exist yet for Saturn. Nonetheless, features suggestive of convection have previously been observed on Saturn, most notably the equatorial Great White Spots but also occasional features at higher latitudes (Smith et al., 1981; Hunt et al., 1982; Sromovsky et al., 1983; Sánchez-Lavega et al., 1991, 2004; Barnet et al., 1992; Beebe et al., 1992; Acarreta and Sánchez-Lavega, 1999).

To date we have not observed a single candidate convective feature in the ISS strong methane band filter MT3 (889 nm), and only one candidate in the moderate strength methane band filter MT2 (727 nm) (see Section 4). We therefore use morphology and temporal evolution of small bright features in the continuum filter CB2 as a qualitative indicator of convective cloud occurrence on Saturn. In several cases ISS acquired simultaneous images in a weak methane band filter (MT1, 619 nm). In each such candidate case identified in CB2, the feature was also visible in MT1, indicating a higher than average cloud top and providing some corroboration of our continuum-only identification of features. Since candidate features must at least stand out as anomalously bright in CB2 to be considered, it is possible that our selection process misses some smaller, shallower convective clouds that do not noticeably differ from other small discrete features. Convective clouds have been surveyed thus far over the periods 6–20 September 2004 (2 × 2 mosaics) and 4–8 (3 × 3 mosaics), 18 (1 × 3 strips), 25–27 February 2005 (1 × 6 strips), during which the pixel resolution ranges from 7 to 100 km pixel^{-1}.

3. Mean flow and eddy momentum fluxes

Fig. 2 shows the geographic sampling of wind vectors obtained using the automated tracking algorithm superimposed on a 360° cylindrical projection of Saturn. Saturn cloud morphology is highly latitude-dependent, with numerous discrete features in the vicinity of the "westward" jets (which are sometimes merely eastward minima on Saturn relative to System III) and lower contrast, more linear striations characterizing the eastward jet latitudes. The latter confound the automated tracking algorithm, producing significantly fewer wind vectors and a much broader distribution of wind speeds than is found elsewhere. We regard the performance of the algorithm as unsatisfactory for the purpose of estimating eddy momentum fluxes at these latitudes, and thus we eliminate most eastward jet regions from our analysis; this explains the latitudinal gaps in Fig. 2. The longitudinal sampling also contains gaps because of our exclusion of images near the terminator and limb during

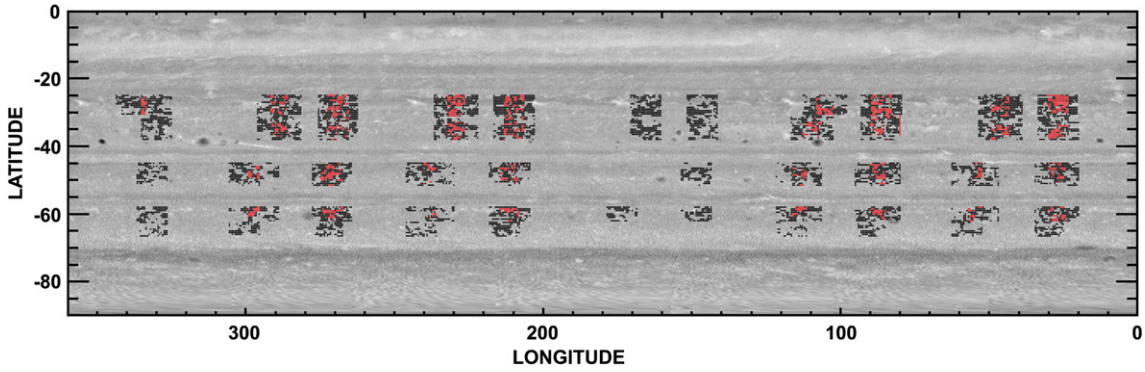

Fig. 2. Geographical distribution of automated tracking wind vectors in the Saturn dataset superimposed on a 360° cylindrical projection of Saturn. Black (pink) dots represent locations of single (multiple) wind vectors.

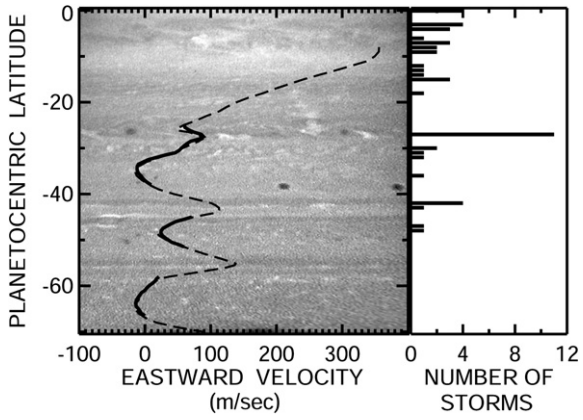

Fig. 3. Left: latitudinal profiles of mean zonal wind from our automated algorithm (solid) and the manual algorithm of Vasavada et al. (2006) (dashed), superimposed on a 750 nm continuum (CB2) Saturn image. Right: latitudinal profile of convective feature occurrence frequency.

the 4 days of observations, rather than because of any inherent properties of the cloud morphology. For the longitudes we can view at favorable geometry, Fig. 2 shows that the sampling is relatively unbiased. Salyk et al. (2006) furthermore show that excluding features such as ovals has little effect on Jupiter eddy momentum flux estimates. Longitudinal sampling should eventually be complete once images from future Cassini orbits are added to the analysis.

Fig. 3 shows the resulting mean zonal wind profile derived from the automated tracking algorithm, compared with that derived by Vasavada et al. (2006) from manual tracking of lower resolution images taken on approach to Saturn in 2004. In general our mean zonal winds are in good agreement (within several $\mathrm{m\,s^{-1}}$) with those of Vasavada et al. (2006). The biggest discrepancies (12–18 $\mathrm{m\,s^{-1}}$) occur equatorward of 30° S near the flanks of the only eastward jet (27.5° S) we retain in our analysis and the transition to the broad equatorial jet, where the automated technique loses reliability. Elsewhere, the biggest difference is that our winds are $\sim$5 $\mathrm{m\,s^{-1}}$ less extreme than those of Vasavada et al. (2006) near the cores of the "westward" jets at 34.5, 48.5, and 64.0° S. This is a more empirical estimate of wind uncertainty, the result being some combination of false identifications by the automated technique and the smaller sampling and coarser resolution images used in the manual tracking analysis.

Letting $\langle x \rangle$ indicate the time and zonal mean value of quantity x, we define deviations of the instantaneous local zonal (u) and meridional (v) winds from the zonal mean as $u' = u - \langle u \rangle$ and $v' = v - \langle v \rangle$, respectively. The eddy momentum flux is then given by $\langle u'v' \rangle$. Fig. 4 shows the latitudinal profiles of mean zonal wind, eddy momentum flux, mean meridional wind, sampling, and root mean square (RMS) wind speed deviations from the mean for our Saturn dataset. At most latitudes retained in our dataset the automated technique successfully tracks $\sim$100–300 features. For all three westward jets (or eastward minima) sampled, the eddy flux changes sign at the jet center. The flux is predominantly equatorward/poleward on the equatorial/polar flanks of each jet, respectively, indicating a systematic transport of momentum away from the jet center. For the one eastward jet we observe, the opposite is true, indicating eddy momentum transport into the jet center. For the 48.5° westward jet, the mean meridional wind suggests convergence into the jet at cloud top, but no such behavior is obvious at the other two westward jets, nor do we see the opposite sense of $\langle v \rangle$ at the 27.5° eastward jet. Instead, $\langle v \rangle$ tends to have a specific sign at the core of the other jets. The RMS wind speed magnitudes are similar to those derived from Voyager images (Sromovsky et al., 1983) and show that the dominant contribution to $\langle u'v' \rangle$ comes from zonal wind fluctuations.

Sromovsky et al. (1982) raised the possibility that the behavior of eddy momentum flux distributions derived from Voyager Jupiter images might be due to a small number of large-magnitude outlier wind vectors whose wind values are not robust to assumptions made in image processing and/or tracking. To investigate this possibility, we have calculated the frequency distribution of individual $u'v'$ values at each latitude. Fig. 5 shows two examples of these frequency distributions on either side of the 48.5° S westward jet, one each at latitudes of strong positive and strong negative $\langle u'v' \rangle$. Values of $u'v'$ of both signs occur at any latitude but the distributions are skewed in a sense consistent with the zonal mean value. The mode value tends to be quite small but also consistent with the sign of the zonal mean. We divide the distribution at each latitude into 3 populations: vectors whose $u'v'$ values fall within one standard deviation of the zonal mean value $\langle u'v' \rangle$, between

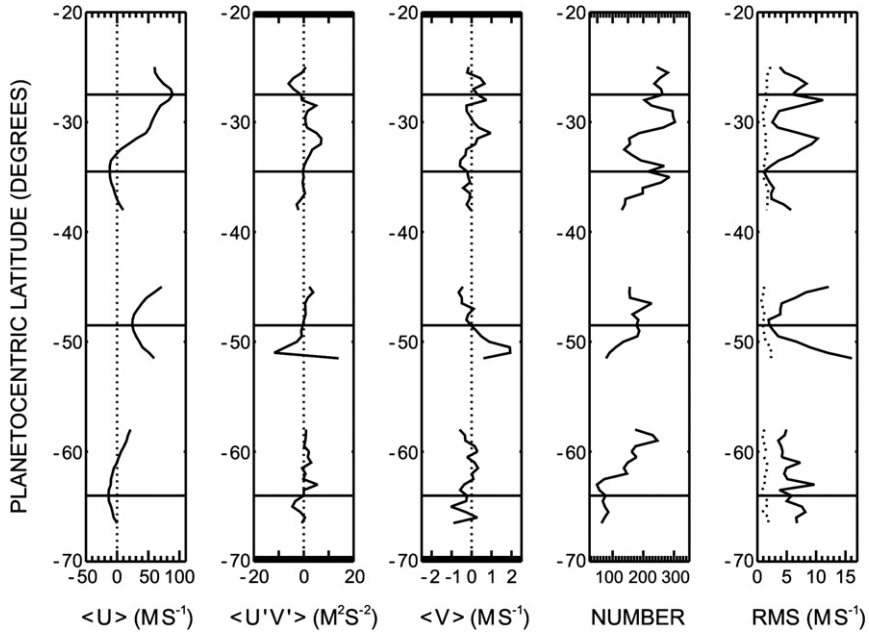

Fig. 4. Latitudinal profiles of (left to right) $\langle u\rangle$, $\langle u'v'\rangle$, $\langle v\rangle$, number of wind vectors, and RMS deviation of u (solid) and v (dotted) at each latitude. Horizontal solid lines denote the locations of jet centers.

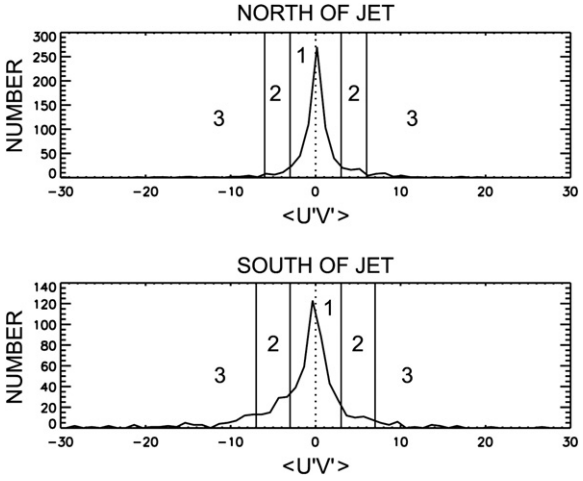

Fig. 5. Frequency distributions of $u'v'$ values, aggregated over three 0.5° latitude bins in each case, just north (upper panel) and south (lower panel) of the 48.5° S westward jet. The vertical lines represent zero wind speed (dotted) and the 1- and 2-standard deviation values (solid) that define populations 1, 2, and 3.

one and two standard deviations, and >2 standard deviations. (Note that Fig. 5 and the subsequent analysis contain only wind vectors that have been judged as successful by the tracking algorithm, i.e., it does not include spurious feature identifications discussed earlier in Fig. 1 whose u or v values are more than a standard deviation away from $\langle u\rangle$ and $\langle v\rangle$ or vectors with correlations <0.5.) A few extreme outliers in each distribution lie beyond the axes in the figure: one value of $+43$ m^2 s^{-2} north of the jet core, and values of $+64$, -35, -41, -42, -69, -107, and -114 m^2 s^{-2} south of the jet core.

Fig. 6 shows examples of the types of features that contribute to the three populations. Populations 1 and 2 appear to be dominated by well-defined cloud features whose motions are correctly diagnosed by the tracking algorithm. Visual inspection of 20 randomly selected samples from each population showed 3 ambiguous cases but no obvious examples of spurious vectors, nor any tendency for the algorithm to preferentially sample one side of a vortex or spot that might bias $u'v'$. Population 3, on the other hand, appears to be a roughly even mixture of real wind vectors, spurious feature tracks not eliminated by our screening criteria, and faint or poorly defined features whose motions are not easily judged. Of the 23 cases whose sign of $u'v'$ is the same as that of $\langle u'v'\rangle$ north and south of the jet in Fig. 5, visual inspection defines 10 as accurate wind vectors, 7 as spurious matches, and 6 as ambiguous. For example, the feature in the lower left panels of Fig. 6 has a value of $u'v' = +20$ m^2 s^{-2} and appears to be a real wind vector associated with a small, possibly convective, feature at 47.5° S. The feature in the lower right panels of Fig. 6 is the one that produces the vector with the largest magnitude $u'v' = -114$ m^2 s^{-2} south of the jet; it is clearly a spurious result. Note that although such vectors make a disproportionate contribution to $\langle u'v'\rangle$, their magnitudes are considerably smaller than those of the Jupiter outliers highlighted by Sromovsky et al. (1982), and their contribution to $\langle u'v'\rangle$ is less because of the large number of wind vectors at each latitude. We attempted to eliminate these spurious outliers by requiring that features give similar wind speeds when tracked forward and backward in time (Salyk et al., 2006). However, this constraint applied to randomly sampled population 2 and 3 vectors rejected twice as many accurately tracked vectors as clearly spurious vectors and thus was not applied to the full dataset.

The rate of conversion of eddy kinetic energy to zonal mean kinetic energy can be estimated by taking the mean of the product $\langle u'v'\rangle \mathrm{d}\langle u\rangle/\mathrm{d}y$ over all latitudes and multiplying by the mass per unit area of the layer in which the energy conversion occurs. We cannot compute the actual global mean conversion rate since we sample only one hemisphere, and primarily westward

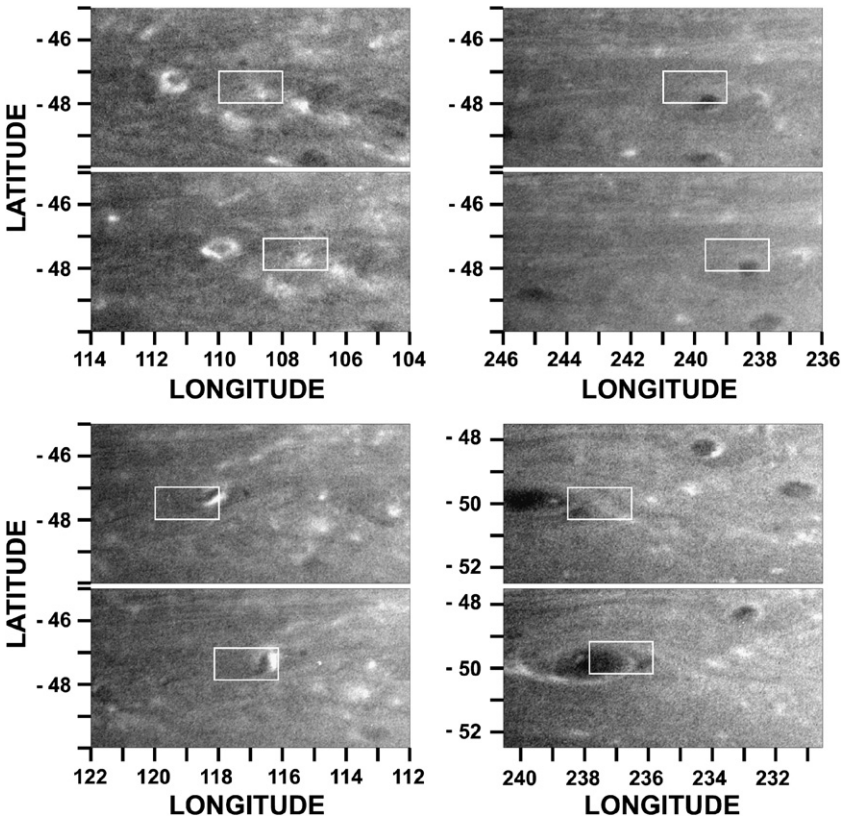

Fig. 6. Upper panels: examples of feature tracks from population 1, with a value of $u'v' = +0.7\ \mathrm{m^2\,s^{-2}}$ (left) and population 2, with a value of $u'v' = +5.0\ \mathrm{m^2\,s^{-2}}$ (right). Lower panels: two examples from population 3, one (left) a real wind vector with $u'v' = +20\ \mathrm{m^2\,s^{-2}}$, and the other (right) a spurious vector that gives a value $u'v' = -114\ \mathrm{m^2\,s^{-2}}$.

jet regions within that hemisphere, and because the relevant layer depth is highly uncertain. With these caveats in mind, we can at least try to make a relative assessment of eddy-mean kinetic energy conversion rates per unit mass on Saturn vs Jupiter. Fig. 4 suggests a generally positive correlation between $\langle u'v' \rangle$ and $\mathrm{d}\langle u \rangle / \mathrm{d}y$. This is illustrated more clearly in Fig. 7, which shows scatter plots of these quantities for the entire nominal dataset and for populations 1, 2, and 3 separately. For the nominal dataset the correlation coefficient is 0.76, comparable to that observed by Salyk et al. (2006) for Jupiter and clearly different from the null result of Ingersoll et al. (1984) from the sparse manually tracked Voyager Saturn sample. To verify that sampling is the primary cause of this difference, we randomly subsampled our dataset to yield a comparable number of vectors (929) to that used in the Voyager Saturn analysis. This reduces the correlation to 0.15, well below the 95% significance level, consistent with the Voyager result. The high correlation in Fig. 7 (upper left) combined with eddy momentum flux magnitudes somewhat smaller than those derived by Salyk et al. (2006) for Jupiter is at least qualitatively consistent with the weaker absorbed and radiated power at Saturn relative to Jupiter.

How eddy momentum fluxes occur and are distributed in space and time is an open question for the jovian planets. On Earth, eddy momentum fluxes are concentrated in a few places such as the North American and Asian storm tracks (Peixoto and Oort, 1991) and occur primarily in the mature stage of baroclinic cyclones (Lau et al., 1978; Del Sole, 2001), i.e., the bulk of the flux occurs in the tails of the frequency distribution. If moist convection is a sporadic source of energy feeding the jets, we might expect eddy momentum fluxes to be sporadic and localized as well. It is therefore natural to ask which of the populations of $u'v'$ vectors in Fig. 5 contributes the most to the observed eddy-mean kinetic energy conversion. The other panels of Fig. 7 show that all three $u'v'$ populations exhibit a positive correlation between $\langle u'v' \rangle$ and $\mathrm{d}\langle u \rangle / \mathrm{d}y$ and thus contribute to eddy-mean kinetic energy conversion: The correlation coefficient between $\langle u'v' \rangle$ and $\mathrm{d}\langle u \rangle / \mathrm{d}y$ is 0.70 for population 1, 0.70 for population 2, and 0.14 for population 3. However, the greater scatter of population 3 only partly offsets the increasing magnitude of $\langle u'v' \rangle$ going from the center to the tails of the distribution. The net result is that the mean $\langle u'v' \rangle\, \mathrm{d}\langle u \rangle / \mathrm{d}y$ for all sampled latitudes is $3.3 \times 10^{-5}\ \mathrm{m^2\,s^{-3}}$ for the nominal dataset, and 0.5×10^{-5}, 5.0×10^{-5}, and 4.5×10^{-5} for populations 1, 2, and 3 respectively.

We also examined the sensitivity of our results to the 0.5 correlation threshold chosen for accepting a successful individual tracking result. The upper panels of Fig. 8 show $\langle u'v' \rangle - \mathrm{d}\langle u \rangle / \mathrm{d}y$ scatter plots for subsets of the data including only vectors with $r > 0.65$ and $r > 0.8$. For the $r > 0.65$ subset the $\langle u'v' \rangle - \mathrm{d}\langle u \rangle / \mathrm{d}y$ correlation is 0.74, quite similar to the result for the nominal dataset. For $r > 0.8$ the correlation is lower (0.48), primarily due to the small number of vectors (<50 at all latitudes) and thus sparse sampling of the $u'v'$ field.

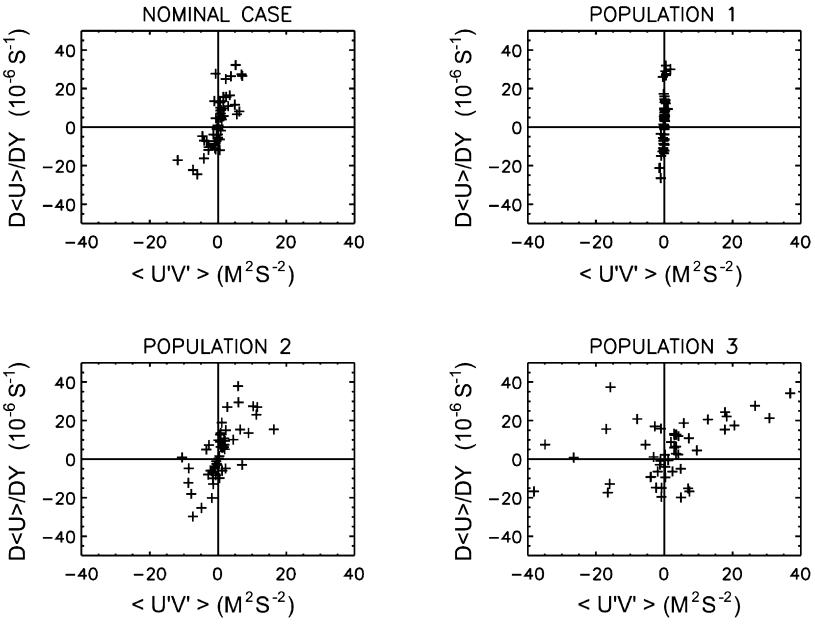

Fig. 7. Scatter plots of $\langle u'v' \rangle$ vs $\mathrm{d}\langle u \rangle / \mathrm{d}y$ for (upper left) the nominal vector population, and for subsets (upper right) population 1, (lower left) population 2, and (lower right) population 3.

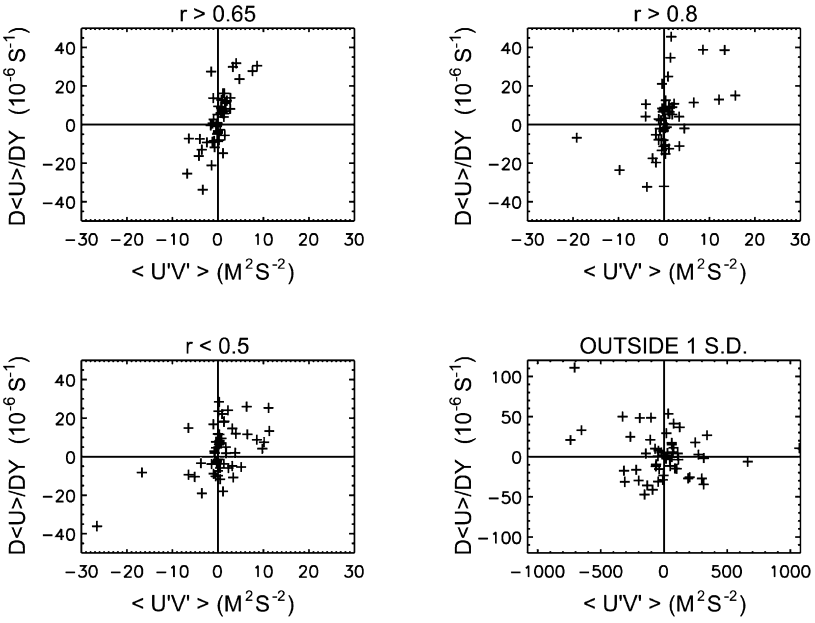

Fig. 8. As in Fig. 7 but for (upper left) a subset of the nominal dataset including only vectors with $r > 0.65$, (upper right) a similar subset including only $r > 0.8$ vectors, (lower left) vectors excluded from the nominal dataset because $r < 0.5$, and (lower right) vectors excluded from the nominal dataset because their u or v values were >1 standard deviation outside the zonal mean.

We next looked at the behavior of vectors excluded by our selection criteria. The vectors excluded because $r < 0.5$ (Fig. 8, lower left) exhibit a correlation of 0.50, still highly significant but considerably lower than that for the nominal dataset. Some of these vectors may be real, and thus it is possible that the magnitude of our estimate of eddy-mean kinetic energy conversion is biased high as a result. On the other hand, $\langle u'v' \rangle$ and $\mathrm{d}\langle u \rangle / \mathrm{d}y$ are not significantly correlated ($r = -0.20$) for the subset of vectors excluded because their u or v values lie more than one standard deviation outside the mean value at a given latitude (Fig. 8, lower right).

Our 2° × 1° target box size is a compromise between the need to adequately resolve the wind profile and the desire to minimize spurious vectors. This box size is larger than the typical discrete feature used in previous manual tracking studies (see Fig. 6). To test this aspect of the difference between the manual and automated approaches, we re-tracked the latitudes north of the 48.5° S jet where strong positive $\langle u'v' \rangle$ occurs with a 1° × 0.5° target box that better captures individual features. With the smaller box, $\langle u \rangle$ changes by $<2\ \mathrm{m\,s^{-1}}$ and $\langle u'v' \rangle$ is ∼25% larger than for the original target size, but ∼80% of the vectors are rejected by our selection criteria.

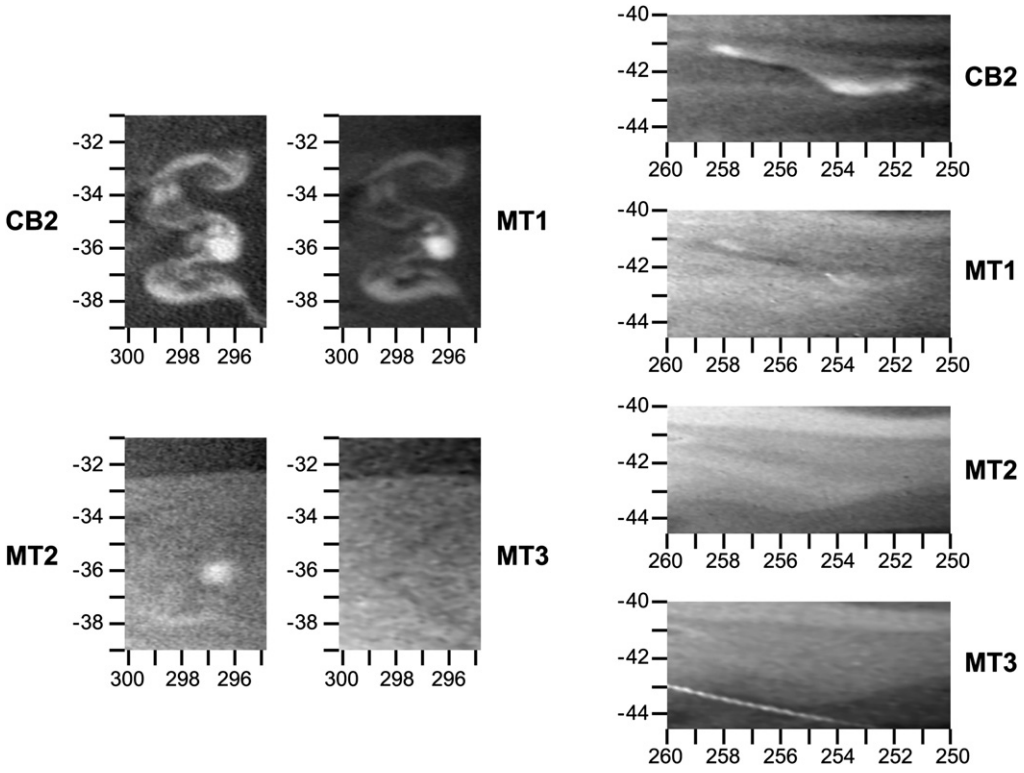

Fig. 9. Two examples of convective feature detection in multiple filters (CB2, 750 nm; MT1, 619 nm; MT2, 727 nm; MT3, 889 nm). Left panels: the 35° S "dragon storm" that coincided with Saturn electrostatic discharge detections. Right panels: a higher latitude (43° S) storm detected near the limb. The bright streak in the mapped MT3 image of the latter storm is a cosmic ray artifact.

Finally, we re-gridded the $u'v'$ data into 1° longitude bins at each latitude, averaged the values in each bin, and then computed $\langle u'v' \rangle$ at each latitude by averaging the mean values for each bin with equal weighting, to reduce the impact of especially well-defined or multiply tracked features that might contribute an inordinate number of vectors to the zonal mean. The $\langle u'v' \rangle$ latitudinal profile of this dataset with less biased sampling (not shown) is almost identical to that of the nominal dataset, with all the primary maxima and minima in $\langle u'v' \rangle$ still present and the magnitude differing by no more than 2 $m^2\,s^{-2}$ at any latitude.

4. Convective feature distribution and evolution

To date we have identified 49 unique candidate convective features, 45 in the Southern Hemisphere where seeing is best and 4 just north of the equator. These occur over ∼3 weeks of imaging, giving an occurrence frequency of ∼2 storms per day over one hemisphere with a mean detection interval of 1–5 rotations between successive storms at a given latitude. Fig. 9 shows two good examples as seen in a variety of ISS filters. The left panels show the "dragon storm" of September 2004, whose appearance and progression across the Saturn disk were observed to coincide with the growth and decay of Saturn electrostatic discharges (Porco et al., 2005), although lightning has not been observed optically for this or any other Saturn storm to date. Although best defined by its optically thick cloud in the continuum filter CB2, it is also clearly visible in the weak methane band MT1 and to a lesser extent in the moderate strength methane band MT2. This storm is the only example to date with an MT2 signature; it does not appear in the strong methane band MT3. Given the estimated Saturn tropospheric haze optical thickness of ∼10 (Karkoschka and Tomasko, 2005), the cloud top for this storm must lie above the bulk of the haze in order for it to be detected at all in MT2. The right panels show one of the more vigorous higher latitude storms (its appearance somewhat distorted by foreshortening) that is visible in CB2 and MT1, but not MT2. The dark feature adjacent to the southern edge of this cloud is either a shadow cast by anomalously high cloud tops or a subsidence-induced clearing of lower-level clouds, either one a sign of vigorous convection. Of the 49 features identified in CB2, 6 were accompanied by MT1 images and all 6 have MT1 signatures as well, lending some confidence to our identification procedure.

Independent evidence for the features we identify actually being convection comes from inspection of their evolution. For 7 of the features observed, we were able to measure the rate of growth either at initiation or early in the storm development over one or two Saturn rotations. For these cases, it is possible to use the observed areal expansion of the bright cloud region to estimate the strength of the underlying cumulus updrafts (Wallace and Hobbs, 2006, p. 310). Assuming that the updraft terminates at cloud top, the mass continuity equation in pressure coordinates relates the vertical flow divergence to the fractional areal rate of expansion, i.e.,

$$\partial\omega/\partial p = -A^{-1}\,\mathrm{d}A/\mathrm{d}t, \tag{1}$$

where ω is the pressure vertical velocity, p is pressure, A is the convective cloud shield area, and t is time. Area was measured by choosing images with a well-defined and stable range of background I/F values, and A was then estimated from the number of pixels that exceed the background I/F (which differs from one case to another but ranges from 0.75 to 0.825). Given two measurements of the area A_1 and A_2 in images separated by time Δt, Eq. (1) can be integrated over the depth D of the layer in which the updraft mass flux converges and combined with hydrostatic equilibrium to give an estimate of the vertical velocity in height coordinates w as

$$w \sim (A_2 - A_1)D/\big[0.5(A_1 + A_2)\Delta t\big]. \quad (2)$$

Assuming a depth $D \sim 100$ km, roughly consistent with the cumulus anvil depth in the cloud—resolving model simulations of Hueso and Sánchez-Lavega (2004), the inferred vertical velocities for the 7 features range from 0.3 to 1.2 m s^{-1}. A more conservative estimate that includes only the area that exceeds the background I/F by a finite amount (∼0.025) and thus more closely captures the convective core region gives velocities of a few m s^{-1} instead. These vertical velocities, which should be interpreted as the mean updraft speed over the mesoscale area of the anvil, are comparable to those derived in similar fashion in previous studies (Hunt et al., 1982; Sánchez-Lavega and Battaner, 1987) and for deep convective storms on Earth (Futyan and Del Genio, 2007). Thus, despite the absence of direct height discrimination for many of the features, all indications are that the features we have selected are actual occurrences of moist convection.

The right side of Fig. 3 shows the frequency distribution of convective feature sightings as a function of latitude. Like that for Jupiter (Porco et al., 2003), convective features on Saturn exist preferentially in cyclonic shear regions (27 of the 45 Southern Hemisphere occurrences) and not at all in anticyclonic shear regions, whose I/F values are clearly lower than those of the features we detect. Tropospheric haze optical thickness varies only slightly on the scale of the jets (Karkoschka and Tomasko, 2005; Pérez-Hoyos et al., 2005), so the occurrence difference is probably real. Unlike Jupiter, a considerable number of features (16) lie close to (within ±1° latitude) an eastward jet, and only 2 near a westward jet [unlike Voyager northern hemisphere images in which westward jets were a preferred convection location (Hunt et al., 1982)]. The Jupiter–Saturn difference might be a product of the greater uncertainty in identifying convective events on Saturn using only CB2 images in many of the cases, but more likely it indicates a real difference in the organization of the circulations on the two planets. Perhaps this should not be a surprise given the weak association of wind and albedo features on Saturn. A considerable number of convective feature candidates are observed in the equatorial zone, but we note that in addition to the 3 × 3 hemispheric mosaics used for cloud tracking, our survey of convective features also includes several strip mosaics of the 0–15° S latitude band that may bias the number of features high relative to more southerly latitudes. On the other hand, tropospheric hazes are optically thicker in the equatorial zone, which may limit feature detection there instead. Convective features were not positively identified poleward of ∼50° S due to a combination of increasing foreshortening, decreasing contrast, and a generally chaotic cloud morphology, but we cannot rule out the possibility of moist convection at high latitudes.

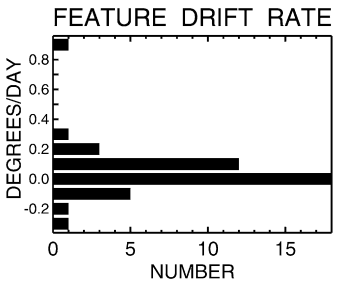

Fig. 10. Frequency histogram of convective feature drift rates measured for all observed multiple occurrences in images separated by one rotation or more.

The fact that convection is common in the cyclonic shear regions of both Saturn and Jupiter raises the question of whether moist convection is indeed the energy source that sustains the jets. As envisioned by Ingersoll et al. (2000), divergence at the convective cloud top produces an anti-cyclonic vortex by geostrophic adjustment that then drifts latitudinally, eventually giving up its energy to the jets. Porco et al. (2005) in fact report tentative evidence of the "dragon storm" giving rise to anticyclonic dark spots. On Earth, cyclones (anti-cyclones) drift poleward (equatorward) under the influence of the planetary vorticity gradient beta (Rossby, 1948; Chan, 2005). On Saturn, however, where the relative vorticity gradient associated with the sheared zonal flow can be of either sign and is 1–5 times beta in the jet regions (see Fig. 10 of Vasavada et al., 2006), the drift direction may not be determined by beta. In addition, the divergent flow at cloud top has its roots in a cyclonic convergent flow at cloud base, and it is not clear which part of the convective system should determine its meridional drift. Fig. 10 shows meridional drift rates estimated from all multiple sightings of Saturn convective features. Most features do not drift at all; for those that do, no preferred direction appears to exist, despite the fact that Saturn convection occurrence prefers eastward to westward jet regions.

We also looked for direct evidence of characteristic features in the $u'v'$ field associated with convective outbreaks. Fig. 11 shows four examples of convective feature sightings that coincided with consecutive rotation image pairs that permit tracking. The color-coded dots overlain on the images indicate the sign and magnitude of coincident $u'v'$ measurements. In general the eddy momentum flux is not unusually large in the vicinity of the convective feature, nor does it appear to have a consistent sign. There were also no indications of unusual behavior in the $u'v'$ field in the same regions after the convection evolved and terminated, in the cases we were able to observe. On the other hand, the small feature in the lower left panel of Fig. 6, which appears bright due to extensive image processing but is actually no brighter than numerous other small-scale features at its latitude and thus was not flagged as a convective candidate (no MT1 image exists to assess vertical development), does exhibit a large positive (out of the 48.5° S westward jet)

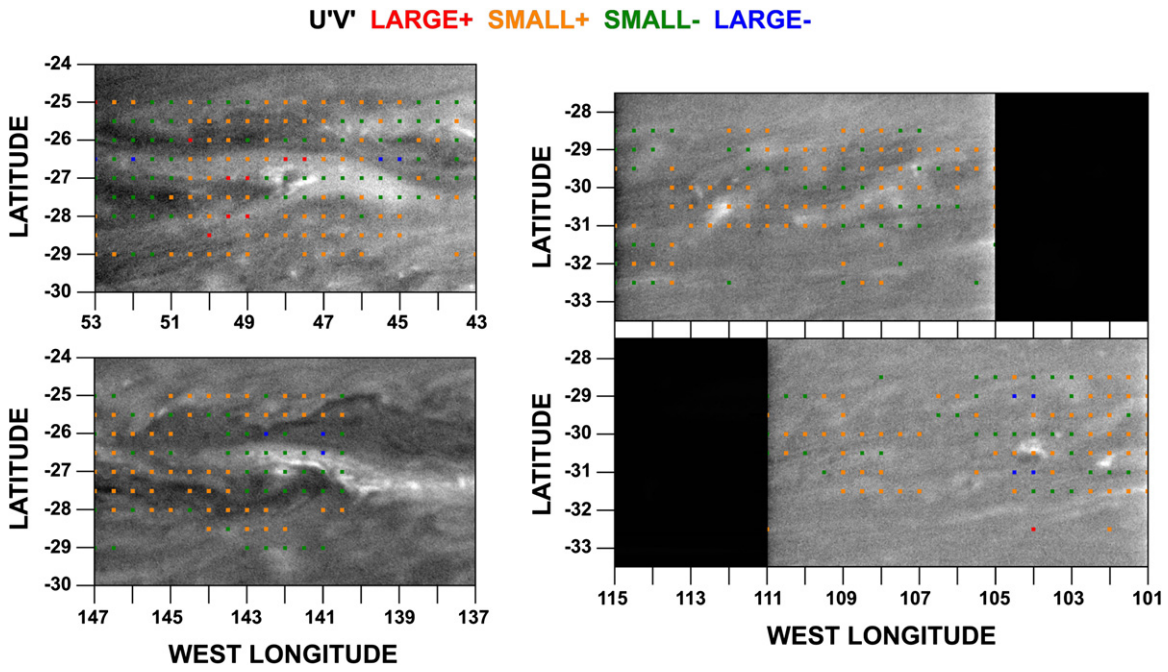

Fig. 11. Four examples of convective features with coincident $u'v'$ patterns overlaid. Large (small) positive $u'v'$ are indicated by the red (orange) dots, and large (small) negative values by the blue (green) dots.

eddy momentum flux. Furthermore, the relative displacements of the bright and adjacent dark features in the image pair suggest some anti-cyclonic vorticity in the immediate vicinity of the feature. Thus, we cannot yet conclusively support nor rule out the convective forcing hypothesis of jet maintenance.

5. Discussion

Our results demonstrate the difficulty of observationally constraining the processes that maintain the jets on jovian planets. The dynamical fluxes of interest may occur infrequently by terrestrial standards, thus necessitating the longer observing baseline possible from an orbiting spacecraft and automated approaches to tracking that maximize image information content. But such techniques are not foolproof when applied to linear or curved cloud morphologies, and the probable skewed nature of the actual flux distribution is difficult to separate objectively from a skewed distribution produced by a small number of spurious feature tracks.

That having been said, our results constitute strong evidence for the existence of a pattern of eddy momentum fluxes that supplies momentum to at least one eastward jet and removes momentum from westward jets on Saturn. Clearly some of the largest wind vector contributions to our estimates of $\langle u'v' \rangle$ are spurious, but just as clearly, some of them are real. The impact of spurious outliers in our dataset is lessened by selection criteria that screen out many of the obvious erroneous cloud pattern matches. Furthermore, the sign of $\langle u'v' \rangle$ is the same for the highest confidence, most frequently occurring population of values as for the largest magnitude outlier population that contains some spurious vectors, while $\langle u'v' \rangle$ for the vectors we exclude also has the same sign but is of smaller magnitude. Finally, convective storms, the most obvious potential source of physically real outliers, do not exhibit unusual values of $u'v'$.

Our most conservative estimate of the mean flow forcing by eddy momentum flux convergence $\partial \langle u \rangle / \partial t = -\partial \langle u'v' \rangle / \partial y$ is obtained by including only those vectors from population 1, which contributes an order of magnitude less to the overall eddy-mean kinetic energy conversion than populations 2 and 3. For population 1, this gives a mean flow acceleration $\mathrm{d}\langle u \rangle / \mathrm{d}t \sim 10^{-6}\ \mathrm{m\,s^{-2}}$ and thus a time scale of replenishing the jets of $\sim$1 yr. For the nominal dataset that includes all three populations, the forcing is $\sim$5 times as strong.

With the exception of the equatorial region, the observed mean flow on Saturn does not evolve on this time scale. Most likely this is because the total flow acceleration depends not only on the horizontal convergence of the eddy momentum flux, but also on unknown contributions from vertical eddy momentum fluxes and the Coriolis force acting on the mean meridional circulation. The last of these can be due to an indirect, Ferrel cell-type overturning response to the eddy momentum flux convergence pattern. If the overturning is indeed associated with the eddy momentum forcing we observe, then in equilibrium $\mathrm{d}\langle u \rangle / \mathrm{d}t \sim 0$ and the first-order momentum balance at cloud level in the center of the jets (where convergence of momentum transport by the mean flow can be neglected) is

$$f \langle v \rangle \sim -\partial \langle u'v' \rangle / \partial y, \tag{3}$$

where f is the Coriolis parameter. Such behavior is seen in jovian planet circulation simulations (Showman et al., 2006). For this scenario to be true upwelling (downwelling) would have to occur in the cyclonic (anti-cyclonic) shear regions. This would be consistent with the observed moist convection asymmetry between cyclonic and anti-cyclonic shear regions, since such a vertical motion pattern would imply moisture convergence

in the cyclonic regions near the water condensation level and destabilization of the lapse rate in the cyclonic regions by adiabatic cooling to promote convective instability. This is the same hypothesis for the flow suggested for Jupiter by Ingersoll et al. (2000) and Porco et al. (2003). Mean upwelling might be possible in the cyclonic regions of both planets, despite lower cloud tops overall there, if the upwelling is concentrated in the small area of the cumulus updrafts themselves and mostly compensated by large-scale subsidence elsewhere, as in Earth's tropics (Zhang et al., 2003). We can only indirectly infer such a pattern, however. The implied mean meridional flow at the upper cloud level would then be from the cyclonic to the anti-cyclonic regions, i.e., equatorward (poleward) across an eastward (westward) jet. The resulting Coriolis torque would decelerate (accelerate) the flow, countering the effect of the eddy momentum flux convergence (divergence).

Meridional winds of the correct sign to support such a hypothesis do occur in our dataset in the vicinity of the 27.5° S eastward jet and the 34.5° and 64.0° S westward jets (Fig. 4), but not at the 48.5° S westward jet, where $\langle v \rangle$ converges instead. [Note that Sromovsky et al. (1983) report mean flow *divergence* instead in one northern hemisphere westward jet during the Voyager era.] However, the magnitudes of the meridional winds ($\sim$1 m s^{-1}) are only slightly greater than our ability to estimate them in the zonal mean. Furthermore, the magnitude of $\langle v \rangle$ required by Eq. (3) is only $\sim$0.02 m s^{-1} for the nominal dataset, and less for population 1 vectors. Thus, it may be premature to claim that we have detected actual mean meridional winds on Saturn. On the other hand, Eq. (3) is a statement of the possible climatological dynamical balance, and there is no need for it to be satisfied on the time scales of a few days that we observe. Indeed, if eddy momentum flux pumping of the jets is episodic, much larger meridional winds may occur episodically as well during the geostrophic adjustment phase.

The above picture, which appears to be consistent with cloud-level observations of Jupiter, is apparently only part of the story for Saturn, since we observe convection preferentially not only in the cyclonic shear regions but also in the eastward jets. If this implies an additional component of upwelling (downwelling) in the eastward (westward) jets, then we would expect upper cloud level divergence (convergence) in these locations, which might explain the derived mean meridional wind pattern near the 48.5° S jet. In this regard it is worth noting that Williams (2003), in a model of thin layer nonlinear baroclinic instability, achieves a pattern consistent with the above picture, including vertical eddy heat fluxes generated at depth in the eastward jet regions, coincident with where we observe convection, and simultaneous eddy momentum fluxes that converge into the eastward jets at higher levels.

The baroclinic instability mechanism allows for eddy fluxes on both sides of the jet, as observed; it is not clear how convective pumping that is restricted to the cyclonic regions would generate eddy transports in the anti-cyclonic regions as well. Models of the convective pumping mechanism achieve mixed results, some generating a jetlike structure (Li et al., 2006) but others simulating an upscale energy cascade that often forms large vortices instead of jets (Showman, 2007). The two mechanisms are not mutually exclusive—perhaps baroclinic instability accounts for the population 1 and 2 $u'v'$ values that occur most often in our dataset, while episodic convection supplies some of the outliers, and perhaps different mechanisms dominate at different latitudes and times, as opposed to the one-explanation-fits-all approach usually taken to try to understand planetary atmospheres. The complex relationships among winds, cloud albedo patterns, and convection and the greater equatorial wind and/or cloud variability on Saturn, relative to Jupiter, might have something to do with Saturn's greater seasonality and its effect on the latitudinal heating gradients that drive the eddies simulated by Williams (2003).

Whatever the mechanism that maintains the jets, the eddy-mean kinetic energy conversion rate per unit mass that we estimate by including all 3 populations of wind vectors is about a factor of two smaller than Salyk et al.'s (2006) near-global mean result for Jupiter. By comparison, Saturn's thermal emission is about a third that of Jupiter, so given our sampling constraints and possible differences in the layer depth of interest, we cannot rule out the possibility that the Jupiter and Saturn circulations are driven with comparable efficiency. The absolute value of the conversion rate on either planet, however, should be considered uncertain by about an order of magnitude, until the nature of outlier vectors is better understood.

The cloud-resolving model simulations of Hueso and Sánchez-Lavega (2004) indicate that updraft speeds for water convection on Saturn should exceed 100 m s^{-1}. If so, this would represent an enormous mass source to the upper troposphere that would almost surely have ramifications for the larger-scale flow. Our results, however, cast these findings into doubt. The convective feature areal expansion rates we measure imply updraft speeds of no more than a few m s^{-1}. Although this result applies to the mesoscale rather than the narrow convective core itself, it is doubtful that our result can be reconciled with such strong core updraft speeds for two reasons: (1) In deep moist convection on Earth, which exhibits similar mesoscale vertical velocities, core updraft speeds never exceed tens of m s^{-1}; (2) The anvil area of the system shown by Hueso and Sánchez-Lavega (2004) is about an order of magnitude greater than the convective core area, and thus if we scale our derived w values by this area ratio, we also derive a core updraft speed no more than a few tens of m s^{-1}. Hueso and Sánchez-Lavega (2004) in fact conducted several simulations with much weaker updraft speeds, by assuming that a substantial fraction of the updraft condensate does not precipitate and instead reduces the buoyancy of the updraft; this may be a more realistic scenario for jovian planet convection. Hueso and Sánchez-Lavega also simulate ammonia storms with weaker updrafts, but these only reach the base of the tropospheric haze even under favorable conditions and are thus probably not the storms we observe.

Some of these questions may be amenable to further study as the Cassini mission proceeds. By the end of the mission we should have complete longitudinal coverage, sampling at least an order of magnitude greater than was possible in this initial study of 4 days of images, perhaps some higher-resolution images of the eastward jets that may make automatic tracking more feasible, and in 2007 our first views of the northern hemi-

sphere in late winter, for comparison with our current summer view of the southern hemisphere. Individual coordinated feature tracks among several instruments may provide anecdotal evidence of heat transports, albeit at a higher altitude than is optimal. Nonetheless, our first analysis of eddy fluxes on Saturn has defined some common ground with its sister planet Jupiter while also documenting some unique properties that will provide fodder for comparative planetology thinking.

Acknowledgments

We thank Mike Allison for numerous helpful discussions, Agustin Sánchez-Lavega and Sanjay Limaye for constructive reviews, and Josh Riley and Nicole Martin for assistance with the design of the image sequences used in this paper. This research was supported by Cassini Project funding of the Imaging Science Subsystem team.

References

Acarreta, J.R., Sánchez-Lavega, A., 1999. Vertical cloud structure in Saturn's 1990 equatorial storm. Icarus 137, 24–33.

Barnet, C.D., Westphal, J.A., Beebe, R.F., Huber, L.F., 1992. Hubble Space Telescope observations of the 1990 equatorial disturbance on Saturn: Zonal winds and central meridian albedos. Icarus 100, 499–511.

Beebe, R.F., Ingersoll, A.P., Hunt, G.E., Mitchell, J.L., Müller, J.-P., 1980. Measurement of wind vectors, eddy momentum transports, and energy conversions in Jupiter's atmosphere from Voyager 1 images. Geophys. Res. Lett. 7, 1–4.

Beebe, R.F., Barnet, C., Sada, P.V., Murrell, A.S., 1992. The onset and growth of the 1990 equatorial disturbance on Saturn. Icarus 95, 163–172.

Carlson, B.E., Rossow, W.B., Orton, G.S., 1988. Cloud microphysics of the giant planets. J. Atmos. Sci. 45, 2066–2081.

Chan, J.C.L., 2005. The physics of tropical cyclone motion. Annu. Rev. Fluid Mech. 37, 99–128.

Del Sole, T., 2001. A simple model for transient eddy momentum fluxes in the upper troposphere. J. Atmos. Sci. 58, 3019–3035.

Dyudina, U.A., Del Genio, A.D., Ingersoll, A.P., Porco, C.C., West, R.A., Vasavada, A.R., Barbara, J.M., 2004. Lightning on Jupiter observed in the H_α line by the Cassini imaging science subsystem. Icarus 172, 24–36.

Futyan, J.M., Del Genio, A.D., 2007. Deep convective system evolution over Africa and the tropical Atlantic. J. Climate, in press.

García-Melendo, E., Sánchez-Lavega, A., 2001. A study of the stability of jovian zonal winds from HST images: 1995–2000. Icarus 152, 316–330.

Gierasch, P.J., Ingersoll, A.P., Banfield, D., Ewald, S.P., Helfenstein, P., Simon-Miller, A.A., Vasavada, A.R., Breneman, H.H., Senske, D.A., and the Galileo Imaging Team, 2000. Observation of moist convection in Jupiter's atmosphere. Nature 403, 628–630.

Hess, S.L., Panofsky, H.A., 1951. The atmospheres of the other planets. In: Malone, T.F. (Ed.), Compendium of Meteorology. Am. Meteor. Soc., Boston, pp. 391–400.

Hueso, S., Sánchez-Lavega, A., 2004. A three-dimensional model of moist convection for the giant planets. II. Saturn's water and ammonia moist convective storms. Icarus 172, 255–271.

Hunt, G.E., Godfrey, D., Müller, J.-P., Barrey, R.F.T., 1982. Dynamical features in the northern hemisphere of Saturn from Voyager 1 images. Nature 297, 132–134.

Ingersoll, A.P., Cuzzi, J.N., 1969. Dynamics of Jupiter's cloud bands. J. Atmos. Sci. 26, 981–985.

Ingersoll, A.P., Beebe, R.F., Mitchell, J.L., Garneau, G.W., Yagi, G.M., Shu, F.H., 1981. Interaction of eddies and zonal flow on Jupiter as inferred from Voyager 1 and 2 images. J. Geophys. Res. 86, 8733–8743.

Ingersoll, A.P., Beebe, R.F., Conrath, B.J., Hunt, G.E., 1984. Structure and dynamics of Saturn's atmosphere. In: Gehrels, T., Mathews, M.S. (Eds.), Saturn. Univ. of Arizona Press, Tucson, pp. 195–238.

Ingersoll, A.P., Gierasch, P.J., Banfield, D., Vasavada, A.R., and the Galileo Imaging Team, 2000. Moist convection as the energy source for the large-scale motions in Jupiter's atmosphere. Nature 403, 630–631.

Karkoschka, E., Tomasko, M., 2005. Saturn's vertical and latitudinal cloud structure 1991–2004 from HST imaging in 30 filters. Icarus 179, 195–221.

Lau, N.-C., Tennekes, H., Wallace, J.M., 1978. Maintenance of the momentum flux by transient eddies in the upper troposphere. J. Atmos. Sci. 35, 139–147.

Li, L., Ingersoll, A.P., Huang, X., 2006. Interaction of moist convection with zonal jets on Jupiter and Saturn. Icarus 180, 113–123.

Little, B., Anger, C.D., Ingersoll, A., Vasavada, A.R., Senske, D.A., Breneman, H.H., Borucki, W.J., and the Galileo SSI Team, 1999. Galileo images of lightning on Jupiter. Icarus 142, 306–323.

Mitchell, J.M., 1982. The nature of large-scale turbulence in the jovian atmosphere, JPL Publication 82-34. Jet Propulsion Laboratory, Pasadena, 286 pp.

Peixoto, J.P., Oort, A.H., 1991. Physics of Climate. AIP Press, New York, 520 pp.

Pérez-Hoyos, S., Sánchez-Lavega, A., French, R.G., Rojas, J.F., 2005. Saturn's cloud structure and temporal evolution from ten years of Hubble Space Telescope images (1994–2003). Icarus 176, 155–174.

Porco, C.C., West, R.A., McEwen, A., Del Genio, A.D., Ingersoll, A.P., Thomas, P., Squyres, S., Dones, L., Murray, C.D., Johnson, T.V., Burns, J.A., Brahic, A., Neukum, G., Veverka, J., Barbara, J.M., Denk, T., Evans, M., Ferrier, J.J., Geissler, P., Helfenstein, P., Roatsch, T., Throop, H., Tiscareno, M., Vasavada, A.R., 2003. Cassini imaging of Jupiter's atmosphere, satellites, and rings. Science 299, 1541–1547.

Porco, C.C., West, R.A., Squyres, S., McEwen, A., Thomas, P., Murray, C.D., Del Genio, A., Ingersoll, A.P., Johnson, T.V., Neukum, G., Veverka, J., Dones, L., Brahic, A., Burns, J.A., Haemmerle, V., Knowles, B., Dawson, D., Roatsch, T., Beurle, K., Owen, W., 2004. Cassini imaging science: Instrument characteristics and capabilities and anticipated scientific investigations at Saturn. Space Sci. Rev. 115, 363–497.

Porco, C.C., Baker, E., Barbara, J., Beurle, K., Brahic, A., Burns, J.A., Charnoz, S., Cooper, N., Dawson, D.D., Del Genio, A.D., Denk, T., Dones, L., Dyudina, U., Evans, M.W., Giese, B., Grazier, K., Helfenstein, P., Ingersoll, A.P., Jacobson, R.A., Johnson, T.V., McEwen, A., Murray, C.D., Neukum, G., Owen, W.M., Perry, J., Roatsch, T., Spitale, J., Squyres, S., Thomas, P., Tiscareno, M., Turtle, E., Vasavada, A.R., Veverka, J., Wagner, R., West, R., 2005. Cassini imaging science: Initial results on Saturn's atmosphere. Science 307, 1243–1247.

Roos-Serote, M., Vasavada, A.R., Kamp, L., Drossart, P., Irwin, P., Nixon, C., Carlson, R.W., 2002. Proximate humid and dry regions in Jupiter's atmosphere indicate complex local meteorology. Nature 405, 158–160.

Rossby, C.G., 1948. On displacements and intensity change of atmospheric vortices. J. Mar. Res. 7, 175–187.

Rossow, W.B., Del Genio, A.D., Eichler, T.P., 1990. Cloud-tracked winds from Pioneer Venus OCPP images. J. Atmos. Sci. 47, 2053–2084.

Salyk, C., Ingersoll, A.P., Lorre, J., Vasavada, A.R., Ewald, S., Del Genio, A.D., 2006. Interaction between eddies and mean flow in Jupiter's atmosphere: Analysis of Cassini imaging data. Icarus 185, 430–442.

Sánchez-Lavega, A., Battaner, E., 1987. The nature of Saturn's atmospheric Great White Spots. Astron. Astrophys. 185, 315–326.

Sánchez-Lavega, A., Colas, F., Lecacheux, J., Laques, P., Parker, D., Miyazaki, I., 1991. The great white spot and disturbances in Saturn's equatorial atmosphere during 1990. Nature 353, 397–401.

Sánchez-Lavega, A., Hueso, R., Pérez-Hoyos, S., Rojas, J.F., French, R.G., 2004. Saturn's cloud morphology and zonal winds before the Cassini encounter. Icarus 170, 519–523.

Showman, A.P., 2007. Numerical simulations of forced shallow-water turbulence: Effects of moist convection on the large-scale circulation of Jupiter and Saturn. J. Atmos. Sci., in press.

Showman, A.P., Gierasch, P.J., Lian, Y., 2006. Deep zonal winds can result from shallow driving in a giant-planet atmosphere. Icarus 182, 513–526.

Smith, B.A., Soderblom, M., Beebe, R., Boyce, J., Briggs, G., Bunker, A., Collins, S.A., Hansen, C.J., Johnson, T.V., Mitchell, J.M., Terrile, R.J., Carr, M., Cook II, A.F., Cuzzi, J., Pollack, J.B., Danielson, G.E., Ingersoll, A., Davies, M.E., Hunt, G.E., Masursky, H., Shoemaker, E., Morrison,

D., Owen, T., Sagan, C., Veverka, J., Strom, R., Suomi, V.E., 1981. Encounter with Saturn: Voyager 1 imaging science results. Science 212, 163–191.

Sromovsky, L.A., Revercomb, H.E., Suomi, V.E., Limaye, S.S., Krauss, R.J., 1982. Jovian winds from Voyager 2. Part II: Analysis of eddy transports. J. Atmos. Sci. 39, 1413–1432.

Sromovsky, L.A., Revercomb, H.E., Krauss, R.J., Suomi, V.E., 1983. Voyager 2 observations of Saturn's northern mid-latitude cloud features: Morphology, motions, and evolution. J. Geophys. Res. 88, 8650–8666.

Sromovsky, L.A., Revercomb, H.E., Krauss, R.J., 1986. Cloud-top meridional momentum transports on Saturn and Jupiter. In: The Jovian Atmospheres, NASA CP-2441. NASA, New York, pp. 129–143.

Vasavada, A.R., Showman, A.P., 2005. Jovian atmospheric dynamics: An update after Galileo and Cassini. Rep. Prog. Phys. 68, 1935–1996.

Vasavada, A.R., Hörst, S.M., Kennedy, M.R., Ingersoll, A.P., Porco, C.C., Del Genio, A.D., West, R.A., 2006. Cassini imaging of Saturn: Southern hemisphere winds and vortices. J. Geophys. Res. 111, doi:10.1029/2005JE002563. E05004.

Wallace, J.M., Hobbs, P.V., 2006. Atmospheric Science: An Introductory Survey, second ed. Academic Press, New York, 483 pp.

West, R.A., Tomasko, M.G., Smith, B.A., Wijesinghe, M.P., Doose, L.R., Reitsema, H.J., Larson, S.M., 1982. Spatially resolved methane band photometry of Saturn. 1. Absolute reflectivity and center-to-limb variations in the 6190-, 7250-, and 8900-Å bands. Icarus 51, 51–64.

Williams, G.P., 2003. Jovian dynamics. Part III: Multiple, migrating, and equatorial jets. J. Atmos. Sci. 60, 1270–1296.

Zhang, C., Mapes, B.E., Soden, B.J., 2003. Bimodality in tropical water vapor. Q. J. R. Meteor. Soc. 129, 2847–2866.